



ARL-TR-8128 • SEP 2017



# A Multiphysics Finite Element and Peridynamics Model of Dielectric Breakdown

by Raymond A Wildman and George A Gazonas

## **NOTICES**

### **Disclaimers**

The findings in this report are not to be construed as an official Department of the Army position unless so designated by other authorized documents.

Citation of manufacturer's or trade names does not constitute an official endorsement or approval of the use thereof.

Destroy this report when it is no longer needed. Do not return it to the originator.

ARL-TR-8128 • SEP 2017

---



# A Multiphysics Finite Element and Peridynamics Model of Dielectric Breakdown

by Raymond A Wildman and George A Gazonas  
*Weapons and Materials Research Directorate, ARL*

<b>REPORT DOCUMENTATION PAGE</b>				<b>Form Approved OMB No. 0704-0188</b>
Public reporting burden for this collection of information is estimated to average 1 hour per response, including the time for reviewing instructions, searching existing data sources, gathering and maintaining the data needed, and completing and reviewing the collection information. Send comments regarding this burden estimate or any other aspect of this collection of information, including suggestions for reducing the burden, to Department of Defense, Washington Headquarters Services, Directorate for Information Operations and Reports (0704-0188), 1215 Jefferson Davis Highway, Suite 1204, Arlington, VA 22202-4302. Respondents should be aware that notwithstanding any other provision of law, no person shall be subject to any penalty for failing to comply with a collection of information if it does not display a currently valid OMB control number.				
<b>PLEASE DO NOT RETURN YOUR FORM TO THE ABOVE ADDRESS.</b>				
<b>1. REPORT DATE (DD-MM-YYYY)</b> September 2017	<b>2. REPORT TYPE</b> Technical Report	<b>3. DATES COVERED (From - To)</b> June 2016–June 2017		
<b>4. TITLE AND SUBTITLE</b> A Multiphysics Finite Element and Peridynamics Model of Dielectric Breakdown			<b>5a. CONTRACT NUMBER</b>	
			<b>5b. GRANT NUMBER</b>	
			<b>5c. PROGRAM ELEMENT NUMBER</b>	
<b>6. AUTHOR(S)</b> Raymond A Wildman and George A Gazonas			<b>5d. PROJECT NUMBER</b> AH80	
			<b>5e. TASK NUMBER</b>	
			<b>5f. WORK UNIT NUMBER</b>	
<b>7. PERFORMING ORGANIZATION NAME(S) AND ADDRESS(ES)</b> US Army Research Laboratory ATTN: RDRL-WMM-B Aberdeen Proving Ground, MD 21005-5066			<b>8. PERFORMING ORGANIZATION REPORT NUMBER</b> ARL-TR-8128	
<b>9. SPONSORING/MONITORING AGENCY NAME(S) AND ADDRESS(ES)</b>			<b>10. SPONSOR/MONITOR'S ACRONYM(S)</b>	
			<b>11. SPONSOR/MONITOR'S REPORT NUMBER(S)</b>	
<b>12. DISTRIBUTION/AVAILABILITY STATEMENT</b> Approved for public release; distribution is unlimited.				
<b>13. SUPPLEMENTARY NOTES</b> primary author's email: <raymond.a.wildman.civ@mail.mil>.				
<b>14. ABSTRACT</b> A method for simulating dielectric breakdown in solid materials is presented that couples electro-quasi-statics, the adiabatic heat equation, and solid mechanics. These equations are coupled in several ways, including a temperature- and electric-field-dependent conductivity model, Joule heating, thermal expansion, Lorentz and Kelvin electrostatic forces, and a damage-dependent permittivity. A finite element approximation is used for the electro-quasi-static problem and peridynamics is used to model fracture in the solid material. Damage to the material may occur either from high temperatures or high strains. The Kelvin force computation used in the method is verified against a 1-D solution and the linearization scheme used to treat the nonlinear conductivity is verified against a fixed-point iteration solution. Finally, several numerical results are presented, including 2-D point-plane problems, a 2-D composite capacitor with a conductive flaw, and a 3-D point-plane problem. The results show that the method is capable of reproducing both channel-like and tree-like breakdown patterns.				
<b>15. SUBJECT TERMS</b> Joule heating, Lorentz force, Kelvin force, electro-quasi-statics, nonlocal methods				
<b>16. SECURITY CLASSIFICATION OF:</b>		<b>17. LIMITATION OF ABSTRACT</b>	<b>18. NUMBER OF PAGES</b>	<b>19a. NAME OF RESPONSIBLE PERSON</b> Raymond A Wildman
<b>a. REPORT</b> Unclassified	<b>b. ABSTRACT</b> Unclassified	<b>c. THIS PAGE</b> Unclassified	UU	44
				<b>19b. TELEPHONE NUMBER (Include area code)</b> 410-306-2232

## **Contents**

---

<b>List of Figures</b>	<b>iv</b>
<b>List of Tables</b>	<b>v</b>
<b>1. Introduction</b>	<b>1</b>
<b>2. Formulation</b>	<b>2</b>
2.1 Physical Model	2
2.2 Coupling	4
2.3 Conductivity Model	5
2.4 Discretization	5
2.5 Linearization	7
2.6 Nonlocal Force Computation	8
2.7 Algorithm	9
<b>3. Verification</b>	<b>10</b>
3.1 Nonlocal Kelvin Force Computation	10
3.2 Linearization	11
<b>4. Results</b>	<b>14</b>
4.1 Flat Electrode	15
4.2 Tree-Like Breakdown	16
4.3 Sharply Pointed Electrode	17
4.4 Composite Capacitor with Conductive Flaw	18
4.5 Point-Plane Geometry in 3-D	19
<b>5. Conclusions</b>	<b>21</b>
<b>6. References</b>	<b>31</b>
<b>List of Symbols, Abbreviations, and Acronyms</b>	<b>33</b>
<b>Distribution List</b>	<b>35</b>

Approved for public release; distribution is unlimited.

## List of Figures

---

Fig. 1	Permittivity a) and potential b) that generate the Kelvin force of Eq. 37	11
Fig. 2	Nonlocal approximation of Kelvin force in 2-D .....	12
Fig. 3	Comparison of Kelvin force computed using FEM and finite differences .....	12
Fig. 4	Error convergence of Kelvin force computed using FEM and finite differences .....	13
Fig. 5	Schematic of the point–plane geometry .....	14
Fig. 6	Convergence of the linearization of Eq. 30 to a fixed-point iteration solution .....	14
Fig. 7	Error in $\mathbf{E}$ of the linearization with a time-step size of 1 ns vs. a fixed-point solution .....	15
Fig. 8	Peridynamic damage in the flat-tipped point–plane model at 4 $\mu\text{s}$ a), 4.5 $\mu\text{s}$ b), 5 $\mu\text{s}$ c), and 5.5 $\mu\text{s}$ d) .....	16
Fig. 9	Temperature a) and conductivity b) in the flat-tipped point–plane model at 5 $\mu\text{s}$ .....	17
Fig. 10	Tree-like breakdown pattern for linear breakdown problem .....	19
Fig. 11	Peridynamic damage in the sharp-tipped point–plane model at 2.5 $\mu\text{s}$ a), 5 $\mu\text{s}$ b), 7.5 $\mu\text{s}$ c), and 10 $\mu\text{s}$ d) .....	20
Fig. 12	Tree-like breakdown pattern for pointed electrode at 1.5 $\mu\text{s}$ .....	21
Fig. 13	Composite parallel plate capacitor model with mesh .....	22
Fig. 14	Magnitude of the electric field for the composite capacitor model at 0.5 $\mu\text{s}$ .....	23
Fig. 15	Peridynamic damage in the composite capacitor model at 5 $\mu\text{s}$ a), 5.5 $\mu\text{s}$ b), and 6 $\mu\text{s}$ c) .....	24
Fig. 16	Temperature in the composite capacitor at 5.5 $\mu\text{s}$ a) and 5.5 $\mu\text{s}$ b) .....	25
Fig. 17	Conductivity in the composite capacitor at 5.5 $\mu\text{s}$ a) and 5.5 $\mu\text{s}$ b) .....	26
Fig. 18	Cylindrical point–plane model (cutaway) .....	27
Fig. 19	Electric-field magnitude a) and conductivity b) in the 3-D point–plane model at 2.2 $\mu\text{s}$ .....	27
Fig. 20	Peridynamic damage in the 3-D point–plane model at 2.25 $\mu\text{s}$ a), 3 $\mu\text{s}$ b), 3.75 $\mu\text{s}$ c), and 4.5 $\mu\text{s}$ d) .....	28
Fig. 21	Peridynamic damage in the 3-D point–plane model at 4.5 $\mu\text{s}$ shown with a threshold on damage a) and temperature b) .....	29

Fig. 22 Damage for the flat-tipped probe in 3-D at 3.3 $\mu$ s .....	30
--	----

## **List of Tables**

---

Table 1 Physical constants .....	18
----------------------------------	----

**INTENTIONALLY LEFT BLANK.**

## **1. Introduction**

---

Dielectric breakdown occurs when a high voltage or field is applied to matter (solid, liquid, or gas) and the material undergoes rapid degradation due to the stripping of electrons from their nuclei. These newly freed electrons form a plasma channel associated with high temperatures and light and sound emission. In solid materials, permanent material failure is seen along the breakdown channel, and secondary fractures may occur in brittle materials due to thermal expansion. This presents a challenging phenomenon to model due to the coupled, multiphysics nature of the problem. Accurate modeling of dielectric breakdown is useful in several applications, including the design of energy-dense capacitors (including structural capacitors<sup>1</sup>), the design of high-power electronic devices, the design of hardened electronics to electromagnetic pulse attack, and so forth. Indeed, the multiphysics approach used here is especially useful for structural capacitors as mechanical loading could be incorporated into a simulation along with electrical loading.

Previously, a dielectric breakdown method was presented that coupled nonlinear electro-quasi-statics, adiabatic heating, and peridynamics using a finite difference approximation of the electro-quasi-static problem with a 1-phase temperature-conductivity dependency.<sup>2</sup> Here, the method is improved by first using a finite element (FE) discretization of the electro-quasi-static problem, and a 2-phase temperature-conductivity material model. As results will show, the simulated breakdown patterns better match experimental breakdown patterns and can reproduce both channel-like and tree-like geometries.

While dielectric breakdown is a challenging modeling problem, there are other attempts in the literature as well, many of which are listed in Reference 2. The purpose of this report is to first give an overview of the formulation of the journal article cited in Reference 2 while highlighting any differences between that method and the updated FE-based method. In addition, the method is verified against other computational methods and several new geometries are modeled.

The remainder of the report is organized as follows: First, Section 2 details the formulation of the method including the physical model, the discretization, and other approximations. Next, Section 3 verifies the proposed method against other computational techniques. Section 4 presents several different examples of the method on different geometries, including 3-D, and finally Section 5 concludes the report.

## 2. Formulation

---

This section details the formulation of the dielectric breakdown problem in terms of 3 coupled partial differential equations. The formulation is similar to that of Reference 2, though it is repeated here for clarity. The main differences are the model used for the temperature dependence of the conductivity and the spatial discretization, which are discussed in Sections 2.3 and 2.4 respectively.

### 2.1 Physical Model

---

The model used here couples 3 field equations: electro-quasi-statics, the adiabatic heat equation, and solid mechanics. First, the electro-quasi-static approximation used has the form

$$\nabla \cdot (\sigma(T, |\mathbf{E}|) \nabla \Phi) + \frac{\partial}{\partial t} \nabla \cdot (\epsilon \nabla \Phi) = 0, \quad (1)$$

where  $\mathbf{E}$  is the electric field,  $\Phi$  is the electrostatic potential,  $T$  is temperature,  $\sigma$  is conductivity, and  $\epsilon$  is permittivity. Note that the equation is nonlinear as the conductivity depends on the potential (via the electric field) and also that the material properties may be spatially inhomogeneous and time-dependent. Next, the temperature dependence is defined as

$$\frac{\partial}{\partial t} T = \frac{1}{c_p \rho} Q - \beta \delta(T - T_c), \quad (2)$$

where  $\delta(\cdot)$  is the Dirac delta function,  $c_p$  is the heat capacity,  $T_c$  is a phase change temperature,  $\beta$  is related to the energy required for the phase change, and  $Q$  is a heat source term, which will be defined in Section 2.2.

Finally, solid mechanics will be used to model forces on a solid body due to thermal expansion and electrostatic forces (Lorentz and Kelvin), though peridynamics will be used rather than standard elastodynamics as we wish to model fracture and failure of a material due to high strains and temperatures. Peridynamics is a nonlocal formulation of elastodynamics that naturally incorporates discontinuities that arise from fracture.<sup>3,4</sup> Bond-based peridynamics may be stated as

$$\rho \frac{\partial^2}{\partial t^2} \mathbf{u} = \int_{\mathcal{H}_x} \mathbf{f}(\mathbf{u}' - \mathbf{u}, \mathbf{x}' - \mathbf{x}, T) dV', \quad (3)$$

where the so-called microforce function is given as

$$\mathbf{f}(\boldsymbol{\eta}, \boldsymbol{\xi}, T) = c [s(\boldsymbol{\eta}, \boldsymbol{\xi}) - \alpha \Delta T] \frac{\boldsymbol{\eta} + \boldsymbol{\xi}}{|\boldsymbol{\eta} + \boldsymbol{\xi}|}, \quad (4)$$

where  $\Delta T$  is the temperature difference relative to ambient  $T_{\text{amb}}$  and  $\alpha$  is the isotropic thermal expansion coefficient. The peridynamic stretch  $s$  is defined as

$$s(\boldsymbol{\eta}, \boldsymbol{\xi}) = \frac{|\boldsymbol{\eta} + \boldsymbol{\xi}| - |\boldsymbol{\xi}|}{|\boldsymbol{\xi}|}, \quad (5)$$

where

$$\boldsymbol{\xi} = \mathbf{x}' - \mathbf{x}, \quad (6)$$

and

$$\boldsymbol{\eta} = \mathbf{u}' - \mathbf{u}, \quad (7)$$

and constant  $c$  is defined as

$$c = \frac{6E}{\pi \delta^3 (1 - \nu)}, \quad (8)$$

for 2-D plane stress, or

$$c = \frac{6E}{\pi \delta^4 (1 - 2\nu)}, \quad (9)$$

for 3-D in terms of Young's modulus  $E$  and Poisson's ratio  $\nu$ . The only difference between this formulation and that in Reference 4 is that isotropic thermal expansion is included.

Damage is modeled in bond-based peridynamics with a bond-breaking scheme, wherein the microforce is set to zero if a pair of points has ever had a stretch that exceeds a given critical value. The microforce is then modified as

$$\mathbf{f}(\boldsymbol{\eta}, \boldsymbol{\xi}, T) = ch(t, \boldsymbol{\xi}) [s(\boldsymbol{\eta}, \boldsymbol{\xi}) - \alpha \Delta T] \frac{\boldsymbol{\eta} + \boldsymbol{\xi}}{|\boldsymbol{\eta} + \boldsymbol{\xi}|}, \quad (10)$$

where the health  $h$  of a given bond may be expressed as

$$h(t, \boldsymbol{\xi}) = \begin{cases} 1 & \text{if } s(t', \boldsymbol{\xi}) - \alpha \Delta T(t') < s_0 \text{ and } T_{\text{avg}}(t') < T_c \text{ for all } 0 < t' < t \\ 0 & \text{otherwise} \end{cases}, \quad (11)$$

and the critical stretch  $s_0$  is

$$s_0 = \sqrt{\frac{4\pi G_0}{9E\delta}}, \quad (12)$$

for 2-D plane stress or

$$s_0 = \sqrt{\frac{5G_0}{6E\delta}}, \quad (13)$$

for 3-D. In Eq. 11, excessive temperature will also fail a bond, and  $T_{\text{avg}}$  is the average temperature of the 2 nodes  $\mathbf{x}$  and  $\mathbf{x}'$  and  $T_c$  is a given critical temperature. Finally, peridynamics has no concept of discrete cracks or fracture surfaces, though damage can be defined as the ratio

$$d = 1 - \frac{\int_{\mathcal{H}_x} h \, dV'}{\int_{\mathcal{H}_x} dV'}. \quad (14)$$

This value is useful for postprocessing and will also be used in a modified permittivity as described in the next section.

## 2.2 Coupling

---

The main field equations (Eqs. 1, 2, and 3) are coupled together in several ways. First, electrostatic forces couple the electric field to the displacement, the first of which is the Lorentz force, defined as

$$\mathbf{F}_L = q\mathbf{E} = \nabla \cdot (\epsilon\mathbf{E})\mathbf{E}, \quad (15)$$

where  $q$  is the charge density. This force acts on free charges in the material in areas of high conductivity. The second force is the Kelvin force, or the force on a dielectric, defined as

$$\mathbf{F}_K = \mathbf{P} \cdot \nabla\mathbf{E} = (\epsilon - \epsilon_0)\mathbf{E} \cdot \nabla\mathbf{E}, \quad (16)$$

where  $\mathbf{P}$  is the polarization and  $\epsilon_0$  is the permittivity of free space. The equation of motion is then modified to

$$\rho \frac{\partial^2}{\partial t^2} \mathbf{u} = \mathbf{F}_{PD} + \mathbf{F}_L + \mathbf{F}_K, \quad (17)$$

where  $\mathbf{F}_{PD}$  is the peridynamic force defined on the right-handside of Eq. 3.

Here, the peridynamic damage is coupled to the permittivity by the linear relationship

$$\epsilon = \epsilon_0 [\epsilon_r (1 - d) + d]. \quad (18)$$

The intent is to model the effect of damage in a material as the formation of voids so that a fully damaged material point (with  $d = 1$ ) acts as free space.

The heat source term  $Q$  in Eq. 2 is derived from Joule heating, or the heat generated from current flowing through a dissipative material, and is given by

$$Q = \mathbf{J} \cdot \mathbf{E} = \sigma |\mathbf{E}|^2. \quad (19)$$

Finally, thermal expansion (defined in Eq. 4) couples the temperature to the mechanical displacement.

### **2.3 Conductivity Model**

---

As mentioned above, the conductivity is dependent on both the electric field  $\mathbf{E}$  and the temperature  $T$ . The model used here is exponential and given by

$$\sigma(T, |\mathbf{E}|) = \sigma_0 f(T) e^{\gamma |\mathbf{E}|}, \quad (20)$$

where  $\sigma_0$  is a base conductivity with zero applied field, and  $f$  is a function describing the temperature dependence.<sup>5</sup> The temperature dependence is a 2-phase Arrhenius model given by<sup>6</sup>

$$f(T) = \begin{cases} A_1 e^{-B_1/T} & T < T_c \\ A_2 e^{-B_2/T} & T \geq T_c \end{cases}, \quad (21)$$

where the  $A_i$  and  $B_i$  are constants of the model. The constants  $A_1$  and  $B_1$  are associated with the weakly conductive phase and  $A_2$  and  $B_2$  are associated with the highly conductive phase, meaning that  $A_1 \ll A_2$ .

### **2.4 Discretization**

---

The spatial discretization of Eq. 3 is a basic collocation method as is used perva-

sively in the literature,<sup>4</sup> given by

$$\mathbf{F}_{\text{PD}} = \sum_{j|\mathbf{r}_j \in \mathcal{H}_{\mathbf{r}_i}}^{N_i} \mathbf{f}\left(\boldsymbol{\eta}_{ij}, \boldsymbol{\xi}_{ij}, \frac{\Delta T_i + \Delta T_j}{2}\right) V_j, \quad (22)$$

where  $V_j$  is the volume of node  $j$ . The temporal discretization is a Velocity Verlet method, given as

$$\begin{aligned} \mathbf{v}^{k+1/2} &= \mathbf{v}^k + \frac{\Delta t}{2} \mathbf{a}^k, \\ \mathbf{u}^{k+1} &= \mathbf{u}^k + \Delta t \mathbf{v}^{k+1/2}, \\ \mathbf{a}^{k+1} &= \frac{\mathbf{F}_{\text{PD}} + \mathbf{F}_{\text{K}} + \mathbf{F}_{\text{L}}}{\rho}, \\ \mathbf{v}^{k+1} &= \mathbf{v}^{k+1/2} + \frac{\Delta t}{2} \mathbf{a}^{k+1}. \end{aligned} \quad (23)$$

The main difference between this work and that of Reference 2 is that the electro-quasi-static equation is solved using a finite element method (FEM). First, the FE formulation is given as

$$\sum_n \phi_n \int_{\Omega_m} \sigma \nabla t_m \cdot \nabla b_n dV + \frac{\partial}{\partial t} \sum_n \phi_n \int_{\Omega_m} \epsilon \nabla t_m \cdot \nabla b_n dV = 0, \quad (24)$$

where the  $b_n$  and  $t_m$  are basis and testing functions respectively,  $\Omega_m$  is the support of the  $m^{\text{th}}$  testing function, and  $\phi_n$  are the nodal potentials. As usual, the region is broken into elements, where here quadrilateral (2-D) and hexahedral (3-D) elements are used with bilinear and trilinear basis and testing functions. Further, the peridynamic nodes are located at the centroids of the elements.

An entry in a system matrix is defined as

$$[\mathbf{D}_a]_{mn} \equiv \int_{\Omega_m} a \nabla t_m \cdot \nabla b_n dV, \quad (25)$$

with  $a$  being a dummy variable representing either  $\sigma$  or  $\epsilon$ . The system matrices are formed in the usual way using assembly of element matrices.

Next, the time dependence of the adiabatic heating model is discretized using ex-

plcit forward Euler as

$$T^{k+1} = T^k + \frac{\Delta t}{c_p \rho} Q^k - \Delta t \beta \delta (T^k - T_c). \quad (26)$$

To facilitate the evaluation of Eq. 26, the delta function is regularized with a Gaussian as follows

$$\delta(t) \approx \frac{1}{\sqrt{\pi}a} e^{-t^2/a^2}, \quad (27)$$

where  $a$  is the variance and is a parameter of the model.

## 2.5 Linearization

---

The electro-quasi-static equation is nonlinear in the potential because the conductivity depends on the magnitude of the electric field. This equation may be solved in a few ways, and here we use a linearization procedure along with a backward Euler temporal discretization. First, the FE-discretized approximation may be expressed as

$$\mathbf{D}_\sigma \Phi + \frac{\partial}{\partial t} \mathbf{D}_\epsilon \Phi = 0, \quad (28)$$

where system matrices  $\mathbf{D}_\sigma$  and  $\mathbf{D}_\epsilon$  are defined in Eq. 25 and  $\Phi$  is a vector of nodal unknowns representing the potential. Now, the temporal derivative is applied to both the potential and the permittivity, as the permittivity is time-dependent (because it depends on peridynamic damage), giving

$$\mathbf{D}_\sigma \Phi + \mathbf{D}_{\epsilon'} \Phi + \mathbf{D}_\epsilon \frac{\partial}{\partial t} \Phi = 0, \quad (29)$$

where  $\epsilon'$  is the temporal derivative of the permittivity. Backward Euler is used to discretize the temporal dependence, giving

$$(\Delta t \mathbf{D}_{\sigma^k} + 2\mathbf{D}_{\epsilon^k} - \mathbf{D}_{\epsilon^{k-1}}) \Phi^k = \mathbf{D}_{\epsilon^k} \Phi^{k-1}. \quad (30)$$

Note that superscript  $k$  indicates the variable at the  $k^{\text{th}}$  time step and that the discretization is also applied to the time derivative on the permittivity.

Now, Eq. 30 may be linearized by expressing the conductivity times the electric

field as a Taylor series about the field at the previous time step, which gives

$$\begin{aligned}\sigma(T^k, |\mathbf{E}^k|) \mathbf{E}^k &\approx \sigma_0 f(T^k) e^{\gamma |\mathbf{E}^{k-1}|} [\mathbf{E}^k \\ &+ \gamma \frac{\mathbf{E}^{k-1} \otimes \mathbf{E}^{k-1}}{|\mathbf{E}^{k-1}|} (\mathbf{E}^k - \mathbf{E}^{k-1})]\end{aligned}\quad (31)$$

Finally, this linearization is inserted into Eq. 30 giving,

$$\begin{aligned}\left( \Delta t \mathbf{D}_{\sigma_1^k} + \Delta t \mathbf{D}_{\sigma_2^k} + 2\mathbf{D}_{\epsilon^k} - \mathbf{D}_{\epsilon^{k-1}} \right) \Phi^k = \\ \left( \mathbf{D}_{\epsilon^k} + \Delta t \mathbf{D}_{\sigma_2^k} \right) \Phi^{k-1},\end{aligned}\quad (32)$$

where  $\mathbf{D}_{\sigma_1^k}$  is the FE matrix associated with the first term on the right-handside of Eq. 31 and  $\mathbf{D}_{\sigma_2^k}$  is the FE matrix associated with the second term. Note that the second term is a tensor, and so the definition of Eq. 25 is extended to

$$[\mathbf{D}_A]_{mn} \equiv \int_{\Omega_m} \nabla t_m \mathbf{A} [\nabla b_n]^T dV. \quad (33)$$

## 2.6 Nonlocal Force Computation

---

The final step in the formulation is the computation of the electrostatic forces  $\mathbf{F}_K$  and  $\mathbf{F}_L$ . Unfortunately, they require that the basis functions be at least twice differentiable (see Eq. 15 and Eq. 16) though here only bilinear (or trilinear in 3-D) basis functions are used. Rather than using a higher-order basis, a nonlocal approximation to the force computation will be used. The following is akin to the state-based peridynamic formulations<sup>7</sup> and concepts from nonlocal calculus.<sup>8</sup>

The first step in computing the electrostatic forces is to compute the electric field  $\mathbf{E}$ , which may be obtained by using the derivative of the basis functions. Here, the field will be evaluated at the centroid of each element, coincident with the peridynamic nodes. Next, the gradient of the field is needed for computing the Kelvin force and is approximated as

$$\nabla \mathbf{E} \approx \left[ \int_{\mathcal{H}_x} c(|\boldsymbol{\xi}|) (\mathbf{E}' - \mathbf{E}) \otimes \boldsymbol{\xi} d\mathbf{x}' \right] \mathbf{K}^{-1}, \quad (34)$$

where  $c(|\boldsymbol{\xi}|)$  is a shape function (which is simply constant over the horizon here) and the same horizon is used as the peridynamic method discussed above, and  $\mathbf{K}$  is

a shape tensor given by

$$\mathbf{K} = \int_{\mathcal{H}_x} c(|\boldsymbol{\xi}|) \boldsymbol{\xi} \otimes \boldsymbol{\xi} d\mathbf{x}'. \quad (35)$$

Finally, the divergence of the electric flux density,  $\mathbf{D} = \epsilon \mathbf{E}$ , is needed to compute the Lorentz force, and is given as

$$\nabla \cdot \mathbf{D} \approx \text{trace} \left\{ \left[ \int_{\mathcal{H}_x} c(|\boldsymbol{\xi}|) (\mathbf{D}' - \mathbf{D}) \otimes \boldsymbol{\xi} d\mathbf{x}' \right] \mathbf{K}^{-1} \right\}. \quad (36)$$

## 2.7 Algorithm

---

To summarize, the previously discussed methods are assembled in the following way:

1. Specify any initial electrical material properties given by the problem geometry and compute initial potential
2. Update the displacement and velocity based on acceleration using Eq. 23
3. Update the temperature using Eq. 26
4. Update the bond health due to stretch and temperature (Eq. 11)
5. Update the permittivity based on the damage using Eq. 18
6. Update the conductivity based on the electric field and temperature using Eq. 31
7. Compute the electrostatic potential ( $\Phi$ ) from Eq. 32, with specified boundary conditions
8. Compute the electrostatic forces from the potential using nonlocal approximations ( $\mathbf{F}_L$  and  $\mathbf{F}_K$ ) with Eq. 15 and Eq. 16
9. Update the velocity and acceleration using all forces  $\mathbf{F}_{PD}$ ,  $\mathbf{F}_L$ , and  $\mathbf{F}_K$
10. Repeat starting at Item 2

This method uses a number of approximations in not only the spatial and temporal discretizations, but also in the computation of the electrostatic forces and other regularizations. It is therefore important to verify various aspects of the method, as discussed in the next section.

### 3. Verification

---

A few approximations used in the approach were verified using other computational methods. First, the computation of the Kelvin force was verified against a Mathematica solution wherein a fictitious force was specified and the permittivity and potential that generate that force were computed. Next, the linearization of the nonlinear conductivity model was verified with a fixed-point iteration scheme.

#### 3.1 Nonlocal Kelvin Force Computation

---

The computation of the Kelvin force uses a nonlocal formulation due to the use of bilinear basis functions, which is verified here using the following approach: First, a fictitious force is specified in 1-D. Next, the permittivity and potential that generate that force are solved numerically. Finally, the permittivity and potential are extended to 2-D (constant along one dimension) and the Kelvin force is computed using the nonlocal approach. The resulting force can then be compared to the original fictitious force.

The force used here has the following form

$$f_K(x) = -10^{-11} \sin \pi x, \quad (37)$$

with  $0 \leq x \leq 1$  and the permittivity  $\epsilon$  and potential  $\phi$  are defined via the coupled ordinary differential equations (ODEs)

$$\epsilon(x) \phi''(x) + \epsilon'(x) \phi'(x) = 0 \quad (38)$$

and

$$\epsilon_0 [\epsilon(x) - 1] \phi'(x) \phi''(x) + f_K(x) = 0, \quad (39)$$

subject to the boundary conditions

$$\begin{aligned} \phi(0) &= 0, \\ \phi(1) &= 1, \\ \epsilon(0) &= 2. \end{aligned} \quad (40)$$

Equations 38 and 39 were solved for permittivity  $\epsilon$  and potential  $\phi$  numerically using Mathematica's built-in ODE solver and are shown in Fig. 1. As stated above, these solutions were extended to 2-D along one dimension and used with the non-

local Kelvin force computation.

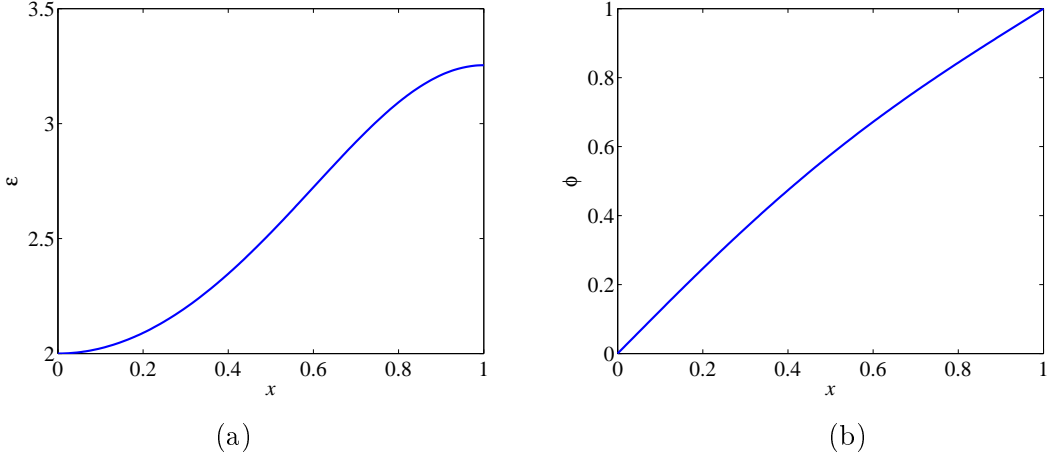


**Fig. 1 Permittivity a) and potential b) that generate the Kelvin force of Eq. 37**

Figure 2 shows the nonlocal approximation of the Kelvin force in 2-D using 100 elements along each axis and a horizon size of  $3\Delta x$ . To compare against the 1-D solution, a slice along the center is used as shown in Fig. 3. Figure 3 also shows the Kelvin force as computed by a finite difference implementation.<sup>2</sup> The error convergence of the Kelvin force computation was also assessed as shown in Fig. 4, where both the finite difference and FE methods are shown. As can be seen, the error in the Kelvin force decreases with an increasing number of elements.

### 3.2 Linearization

---

The linearization described above was verified against a fixed-point iteration solution of the system of equations given in Eq. 30. To perform the fixed-point iteration, Eq. 30 is first rewritten as

$$\mathbf{F}(\Phi)\Phi = \mathbf{b}, \quad (41)$$

where  $\mathbf{F}$  is the matrix defined on the left-handside of Eq. 30 and is a function of  $\Phi$ , and  $\mathbf{b}$  is the right-handside of Eq. 30. This leads to the fixed-point iteration

$$\Phi^{l+1} = \mathbf{F}(\Phi^l)^{-1}\mathbf{b}, \quad (42)$$

and superscript  $l$  refers to a step in the fixed-point iteration, not the time step. This iteration was found to converge if the problem was well-behaved (i.e., at low enough

voltages so that no damage occurred).

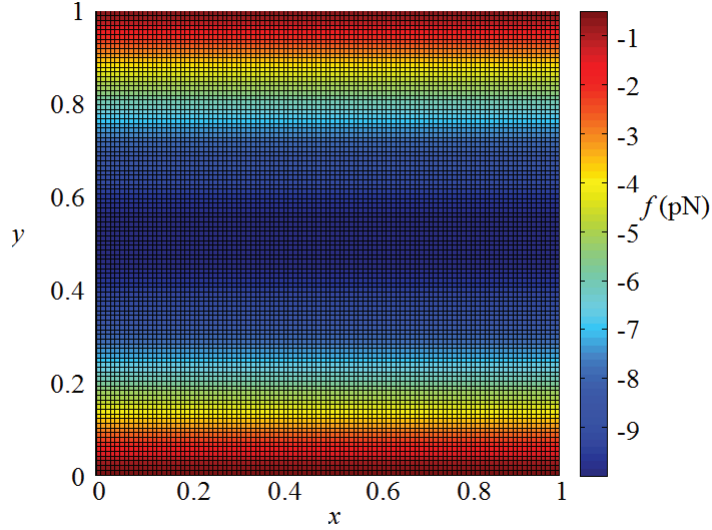


**Fig. 2 Nonlocal approximation of Kelvin force in 2-D**

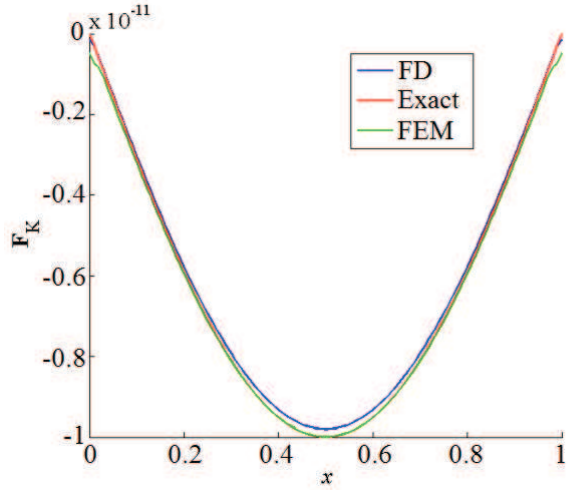


**Fig. 3 Comparison of Kelvin force computed using FEM and finite differences**

For comparison, the fixed-point iteration solution was used rather than the linearization scheme at a timestep size of 125 ps for the point-plane geometry shown in Fig. 5. Only the blue region (dielectric) of Fig. 5 was meshed and an average element edge length of 50  $\mu\text{m}$  was used. The gold regions represent perfect conductors and are boundary conditions in the model. A homogeneous Neumann boundary

condition was used on the dielectric-free space interfaces (top, left, and right edges). In addition, the applied voltage had the form

$$\Phi_{\text{applied}}(t) = V_{\max} (1 - e^{-t/\tau}), \quad (43)$$

where time constant  $\tau$  is 0.3  $\mu\text{s}$  unless specified otherwise.

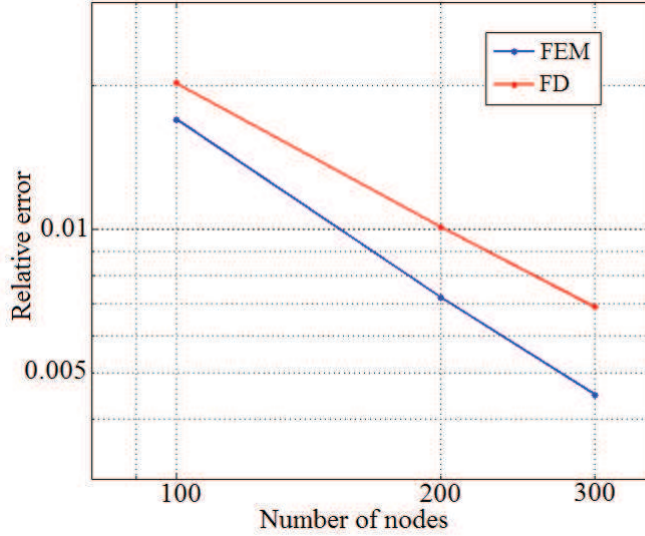


**Fig. 4 Error convergence of Kelvin force computed using FEM and finite differences**

The linearized version was then run at 3 discretizations to a final time of 100 ns: 1 ns, 500 ps, and 250 ps. At the time step corresponding to 100 ns (800 for the fixed-point solution and 100, 200, or 400 for the linearization) the error in the electric field distribution was measured relative to the fixed-point iteration solution. Figure 6 shows the convergence of the linearization to the fixed-point solution for the 3 time-step sizes. As can be seen from the figure, decreasing the time-step size improves the accuracy of the linearized solution. Finally, Fig. 7 shows the log error in  $\mathbf{E}$  of the linearized solution with a 1 ns time-step size after 100 ns. As expected, the error is highest near the highest field concentration, which is where the conductivity will have the highest variation.

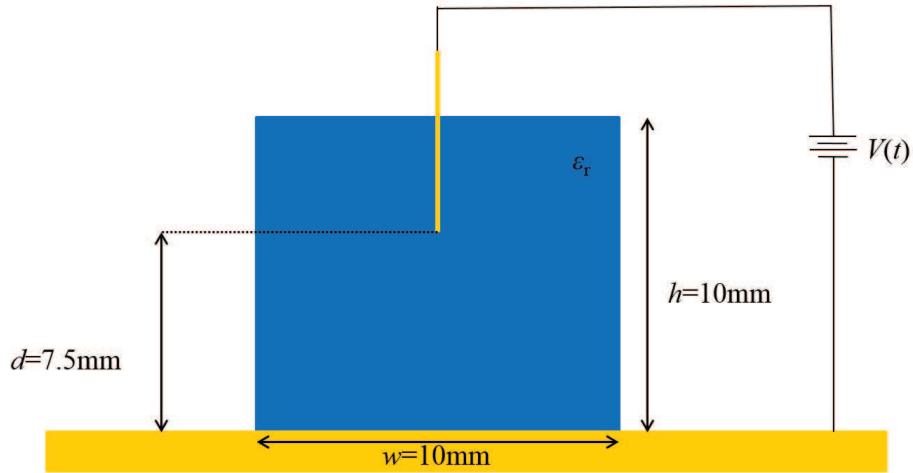


**Fig. 5 Schematic of the point–plane geometry**

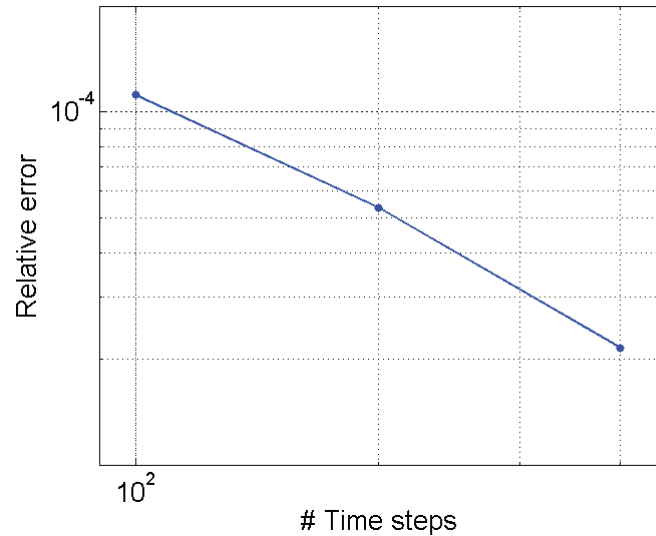


**Fig. 6 Convergence of the linearization of Eq. 30 to a fixed-point iteration solution**

#### 4. Results

---

As a first set of tests, point–plane geometries—wherein a point probe is embedded in a dielectric and placed above a ground plane—were modeled. First, a flat-tipped electrode was modeled twice, first with material properties that generate a straight channel-like breakdown pattern, and second with properties that generate a tree-

like structure. Next, a sharply tipped electrode is modeled. The last 2-D example is a parallel plate capacitor with a composite dielectric and a small conductive flaw. Finally, a 3-D point–plane geometry is tested with a cylindrical dielectric.

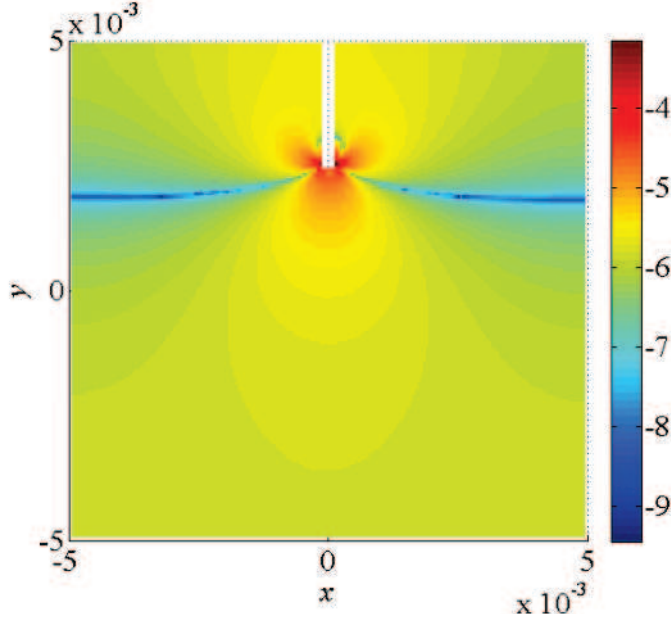


**Fig. 7** Error in  $E$  of the linearization with a time-step size of 1 ns vs. a fixed-point solution

Unless specified otherwise, all material properties used in this section are given in Table 1 and the applied voltage has the form given in Eq. 43.

#### 4.1 Flat Electrode

---

This example repeats the results from Reference 2, though now with the 2-phase model described previously (a schematic of the geometry is shown in Fig. 5). Aside from the 2-phase temperature-conductivity relation, the material properties and geometry are identical to those described in Reference 2. A mesh of quadrilateral elements is used, with average edge length of 50  $\mu\text{m}$ .

The results are shown in the following set of figures: Fig. 8 shows the peridynamic damage at 4 time steps between 4 and 5.5  $\mu\text{s}$  and Fig. 9 shows the temperature and conductivity at 5  $\mu\text{s}$ . Note that the conductivity is shown on a logarithmic scale.

In contrast to the results in Reference 2, a more clearly defined breakdown channel is formed, most likely due to the 2-phase model used for the temperature-

conductivity dependence. Perpendicular fractures are also seen, which are due to the thermal expansion in the breakdown channel applying a force to the surrounding material. This effect is seen in dielectric breakdown experiments.<sup>9</sup>

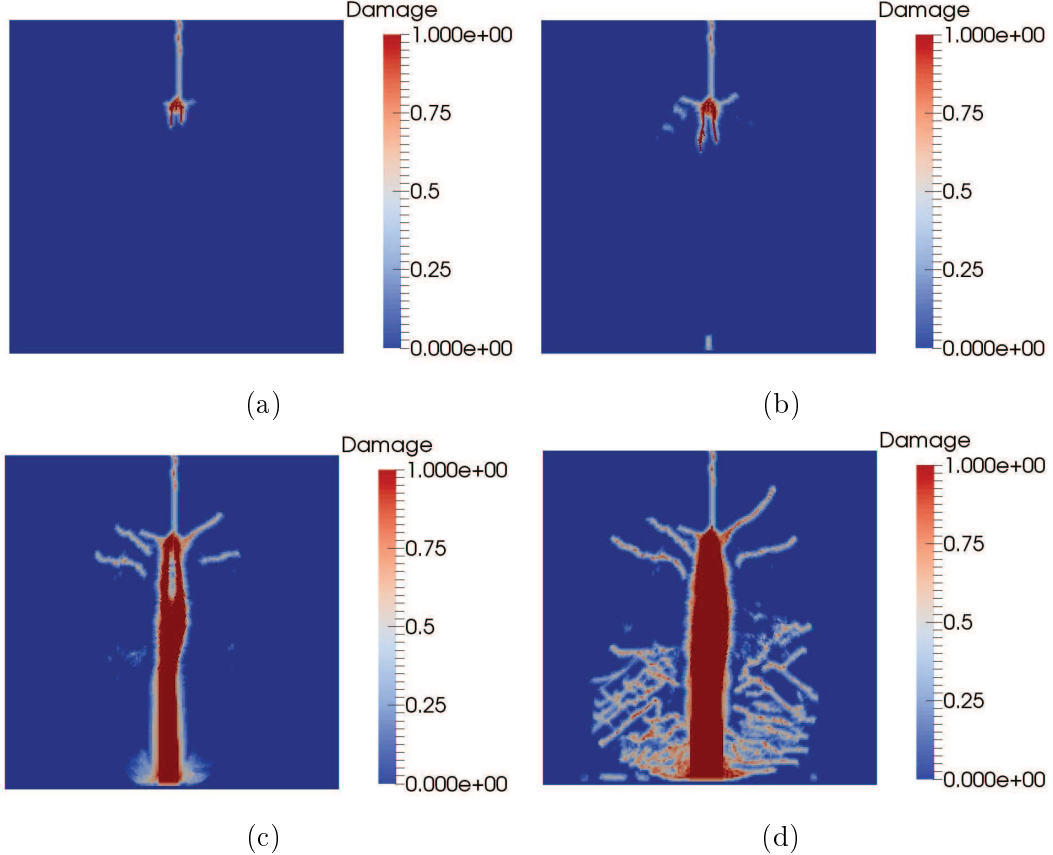


**Fig. 8 Peridynamic damage in the flat-tipped point–plane model at 4  $\mu$ s a), 4.5  $\mu$ s b), 5  $\mu$ s c), and 5.5  $\mu$ s d)**

## 4.2 Tree-Like Breakdown

The same geometry was used as in the previous example, though now the following material properties were altered: The electric field-conductivity coupling coefficient was set to  $\gamma = 0$ , the ambient temperature was increased to  $T_{\text{amb}} = 670$  K, the maximum voltage was  $V_0 = 50$  kV, and the initial conductivity was raised to  $\sigma_0 = 1$  S/m. Note that now the electro-quasi-static equation is linear. These material properties lead to the tree-like breakdown pattern seen in Fig. 10, which shows the peridynamic damage at 1.76  $\mu$ s. It is hypothesized that the tree-like pattern (versus the straighter, channel-like pattern seen in Fig. 8) is because the nonlinearity in the previous example generates a channel of high conductivity, and breakdown can

only occur in this channel. In this example, breakdown may occur anywhere due to the high conductivity throughout the material and so a tree-like pattern develops. Further, the stochastic, unstable damage pattern is most likely due to the irregular mesh.

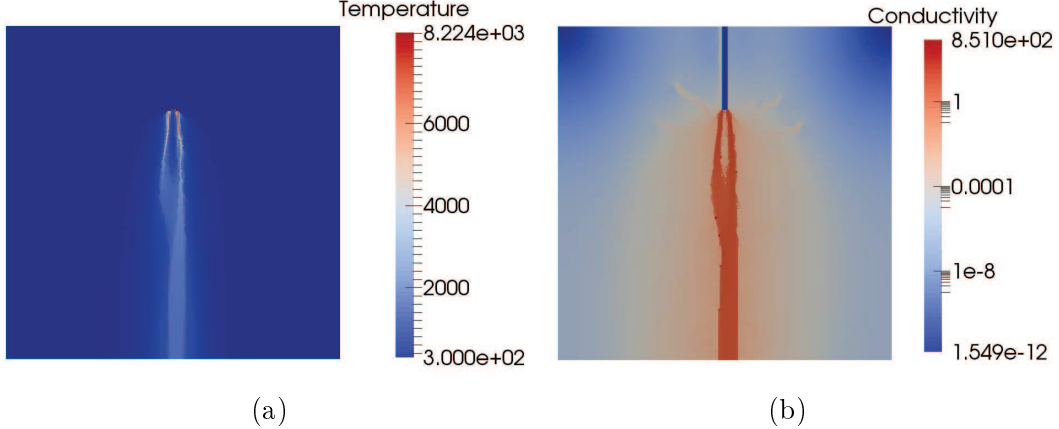


**Fig. 9** Temperature a) and conductivity b) in the flat-tipped point–plane model at 5  $\mu$ s

### 4.3 Sharply Pointed Electrode

Here, nearly the same model as that discussed in Section 4.2 is presented, though now the tip of the electrode is sharp rather than flat. Overall, the results are nearly the same, though the breakdown channel is thinner at first. In addition, breakdown occurs over a longer period of time versus the flat-tipped model. The peridynamic damage is shown in Fig. 11 between 2.5 and 10  $\mu$ s.

The same input parameters from the tree-like breakdown simulation discussed in the previous section were repeated, resulting in the damage pattern shown in Fig. 12. Again, a tree-like pattern is seen, though now only one branch originates from the electrode tip. As before, it is believed that the unstable, tree-like damage pattern is due to the irregular mesh.

**Table 1 Physical constants**

Constant	Value	Units
Mechanical		
$\rho$	2400	$\text{kg m}^{-3}$
$E$	72	GPa
$\delta$	0.15	mm
$G_0$	5	$\text{J m}^{-2}$
Electrical		
$\epsilon_0$	$8.85 \times 10^{-12}$	$\text{F m}^{-1}$
$\epsilon_r$	20	—
$\sigma_0$	$10^{-19}$	$\text{S m}^{-1}$
Thermal		
$c_p$	800	$\text{J kg}^{-1} \text{K}^{-1}$
$T_c$	300	K
$T_{\text{amb}}$	1000	K
Coupled		
$\alpha$	$9 \times 10^{-6}$	$\text{K}^{-1}$
$\gamma$	$5 \times 10^{-8}$	$\text{m V}^{-1}$
$a$	5	K
$\beta$	$8 \times 10^7$	$\text{K}^2$
$A_1$	30	—
$A_2$	$3 \times 10^4$	—
$B_1, B_2$	$1.2 \times 10^3$	K

#### 4.4 Composite Capacitor with Conductive Flaw

---

The final 2-D example is a parallel-plate capacitor with a composite dielectric. The model used 2 dielectric materials along with a small, conductive flaw in the inner dielectric, as shown in Fig. 13, and the conductors were located along the top and bottom edges. The model is 15 mm by 10 mm with a 3-mm-radius circular dielectric located at the center. The outer region had a relative permittivity of 10 and a thermal expansion coefficient of  $9 \times 10^{-6}$  and the inner region had a relative permittivity of 20 and a thermal expansion coefficient of  $20 \times 10^{-6}$ . Within the inner dielectric is a circular, conductive inclusion (conductivity  $10^{-3} \text{ S/m}$ ) with a radius of 75  $\mu\text{m}$ . In addition to having different dielectric constants, the 2 materials had different thermal expansion coefficients to induce fracture at the interface. The maximum voltage used in this simulation was 4 MV with the same time constant used previously.

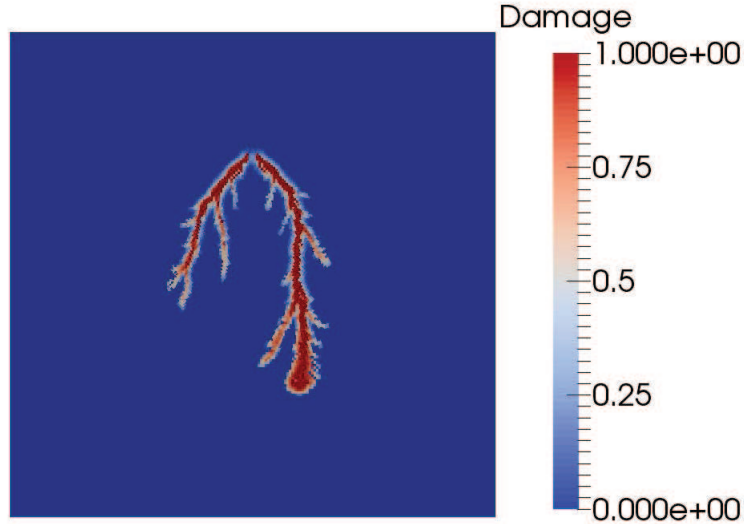


**Fig. 10** Tree-like breakdown pattern for linear breakdown problem

In this model, breakdown initiates at the inclusion, since the inclusion concentrates the electric field (as shown in Fig. 14) at a small point. The breakdown then propagates towards the boundaries as shown in Fig. 15. This damage is associated with high temperatures due to breakdown, though there are other fractures induced by thermal expansion visible especially around the inner dielectric. Finally, the temperature and conductivity are shown in Fig. 16 and Fig. 17. Note that the conductivity is shown on a log scale.

#### 4.5 Point-Plane Geometry in 3-D

---

A 3-D model was generated (shown in Fig. 18), which consisted of a sharply pointed probe of length 1 mm and radius 0.1 mm embedded in a dielectric cylinder with a height of 4 mm and a radius of 2 mm. As before, the voltage is applied to the probe, while the entire bottom surface of the cylinder is the ground plane. While the material properties were the same as above, the temporal discretization was reduced to  $\Delta t = 0.75$  ns and the maximum voltage was reduced to 1.1 MV. The results show a thin breakdown channel forming at approximately 375 ns and propagating more slowly than the 2-D results. First, the electric-field magnitude and conductivity (on a logarithmic scale) are shown in a cutaway view of the dielectric at 2.2  $\mu$ s in Fig. 19. Next, Figure 20 shows a cutaway view of the peridynamic damage in the center of the cylinder at 4 instances of time between 2.2  $\mu$ s and 4.5  $\mu$ s. Compar-

ing Fig. 19b with Fig. 20a shows the peridynamic damage that is associated with breakdown, and not other effects such as thermal expansion. Further, a threshold view of the peridynamic damage is shown in Fig. 21 at 4.5  $\mu$ s, first in a) with a threshold on the damage of 0.25 and second in b) with a threshold on temperature (1000 K). In other words, Fig. 21b shows the damage in regions with high temperature, above the specified breakdown temperature threshold. The difference between the 2 figures illustrates the different types of damage: The thin channel in Fig. 21a is due to high temperature (resulting from high conductivity as shown in Fig. 21b) and the fractures at the bottom of the cylinder are due to thermal expansion as the temperature in that region is below the breakdown threshold.

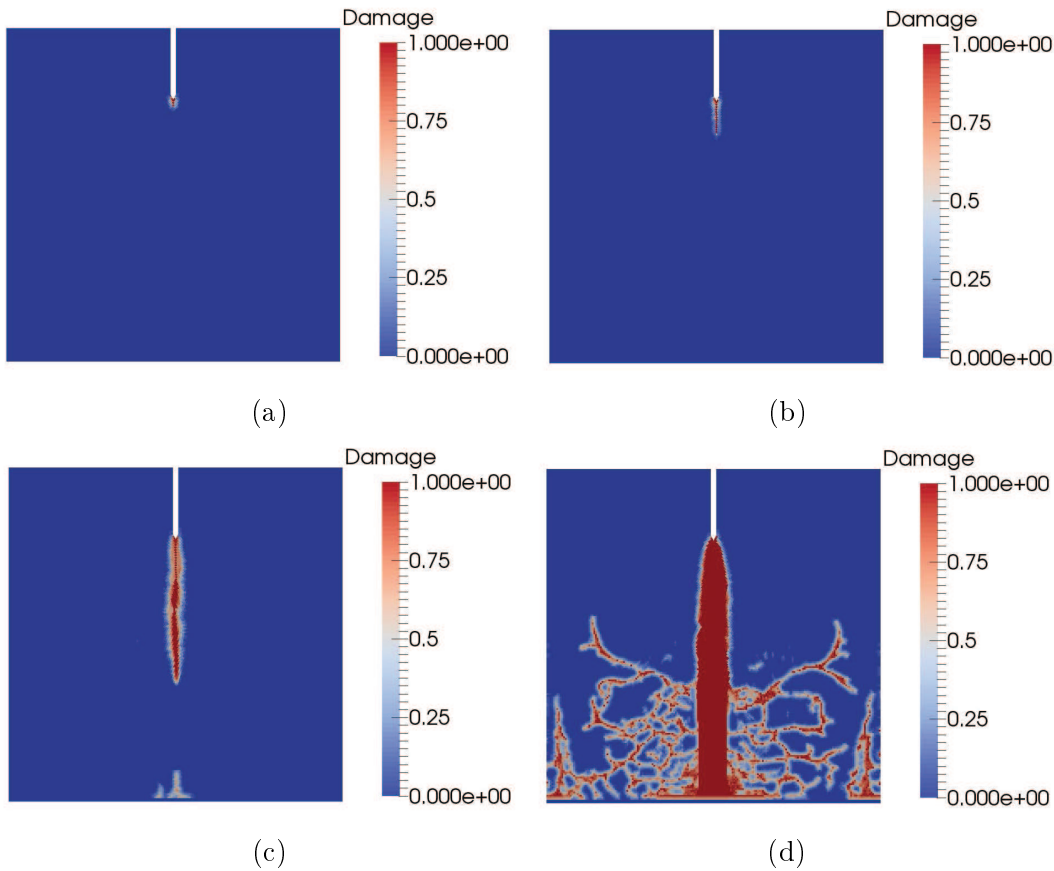


**Fig. 11 Peridynamic damage in the sharp-tipped point–plane model at 2.5  $\mu$ s a), 5  $\mu$ s b), 7.5  $\mu$ s c), and 10  $\mu$ s d)**

Finally, a tree-like breakdown pattern was generated in 3-D by first using a flat-tipped electrode embedded in a dielectric cylinder with the dimensions the same as those stated previously. In this case, the spatial discretization size was reduced

to an average element-edge length of 40  $\mu\text{m}$ . The material properties and initial temperature were the same as those in the tree-like breakdown example in 2-D, though here a maximum voltage of 10 kV was used. Figure 22 shows the damage at 3.3  $\mu\text{s}$  by superimposing a threshold view of the damage (with a threshold of 0.35) on a cut-away view of the damage. As before, a tree-like breakdown pattern is evident that initiates at the flat-tipped electrode.

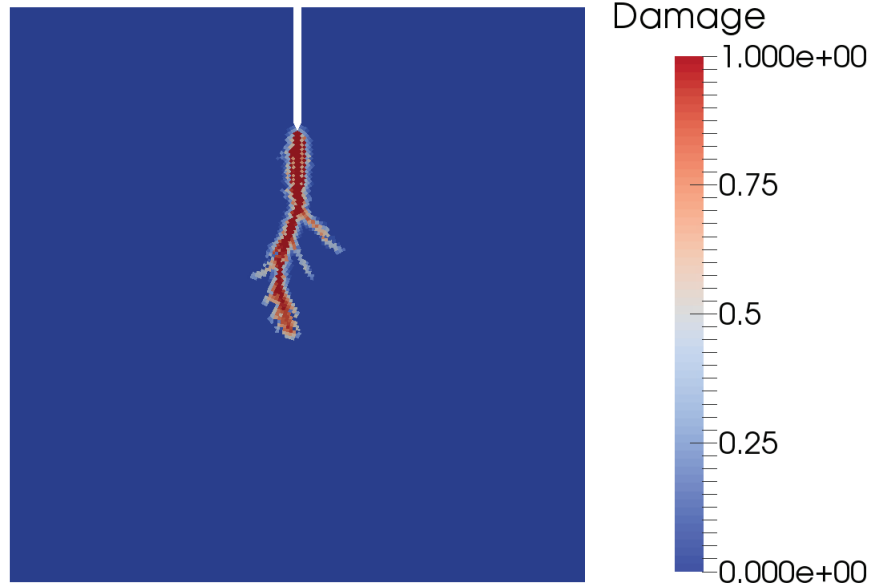


**Fig. 12** Tree-like breakdown pattern for pointed electrode at 1.5  $\mu\text{s}$

## 5. Conclusions

---

A multiphysics, hybrid FE-peridynamics method was presented for solving dielectric breakdown problems. The method coupled 3 field equations: electro-quasi-statics for solution of the electrostatic potential, adiabatic heating for solution of the temperature, and peridynamics for displacement. These 3 equations were coupled in various ways: Lorentz and Kelvin electro-static forces, a temperature- and electric-field-dependent conductivity model, damage-dependent permittivity, and Joule heating. Results were presented for different geometries in 2-D and 3-D and some characteristics were consistent with experiments. The most encouraging result is that the method is capable of generating both channel-like and tree-like breakdown geometries depending on the material properties chosen. The channel-like solutions were generated using the nonlinear electric-field-conductivity dependence

and low initial conductivity and temperature. For the point-probe geometries, it appears the field configuration raises the conductivity along a straight path between the electrode and ground plane, thus only allowing breakdown in this area. The tree-like solutions were generated with a constant conductivity and high initial conductivity and temperature. In this case, the higher background conductivity allows for breakdown to occur on different, unstable paths. These results compare well to Lichtenberg figures, some of which are generated by bombarding a polymer plate with electrons and subsequently applying a large voltage. The embedded electrons raise the charge in the material, which is similar to raising its conductivity.

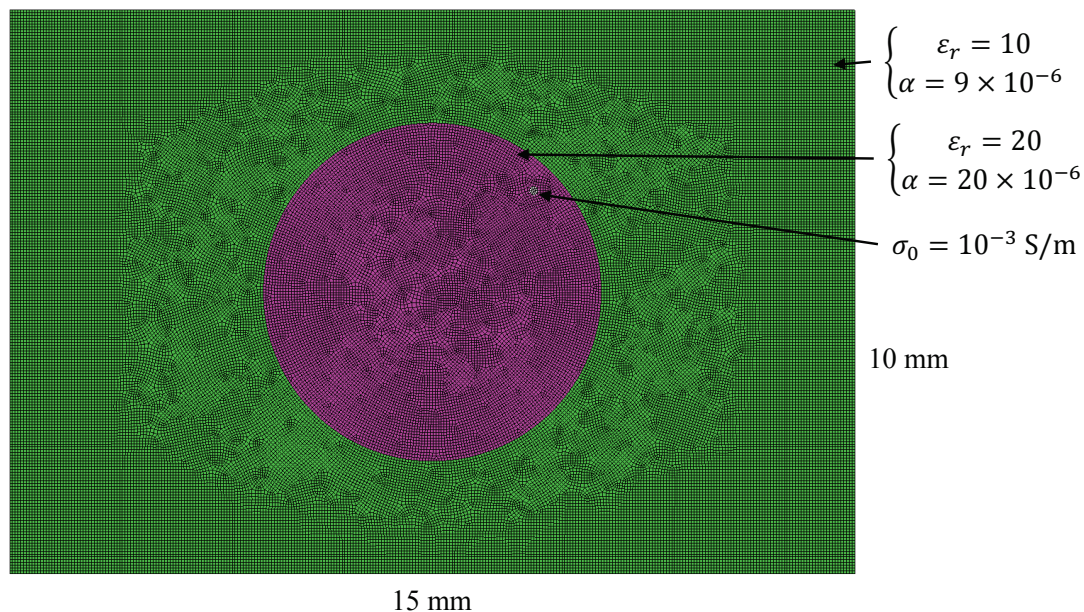


**Fig. 13 Composite parallel plate capacitor model with mesh**

While this approach has generated results that resemble experiments, several improvements could be made. First, the displacement is not coupled to the electrostatic problem, meaning the deformation of the body does not affect the solution of the electro-static problem. In the materials used here, the displacements are small enough to be neglected, though for different materials, such as electro-active polymers, large deformations would necessitate more accurate handling of this coupling. Second, only a 2-phase model is used for the temperature-conductivity dependence, representing low and high conductivity. In reality, a solid undergoing dielectric breakdown may transition through all phases of matter, from solid to liq-

uid, gas, and plasma. Future implementations may incorporate material models for each phase, not just in the temperature-conductivity dependence, but also in the equation of motion and elastic and thermal material properties. Third, the nonlinear electric-field-conductivity dependence is based on experimental support that may not cover the entire range of electric-field magnitudes used here, and so in the future more sophisticated field-dependent conductivity models should be explored. Finally, magneto-static forces may also be included, though it remains to be seen whether or not the magnitude of such forces would impact the solution.

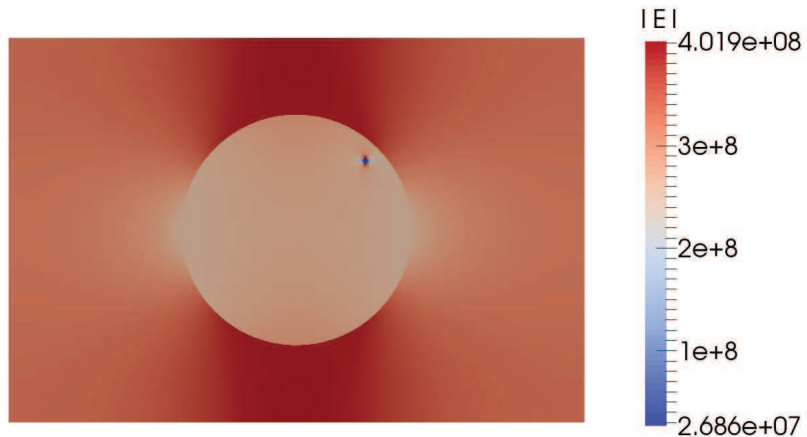
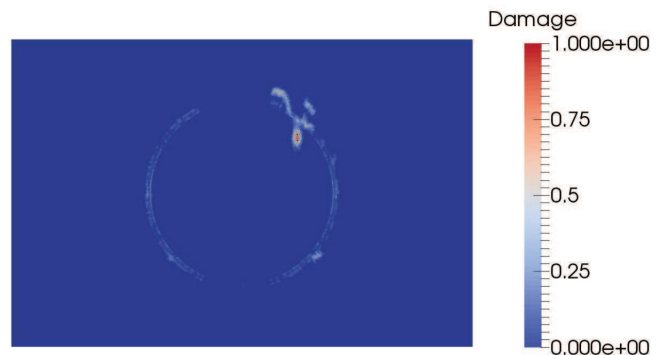
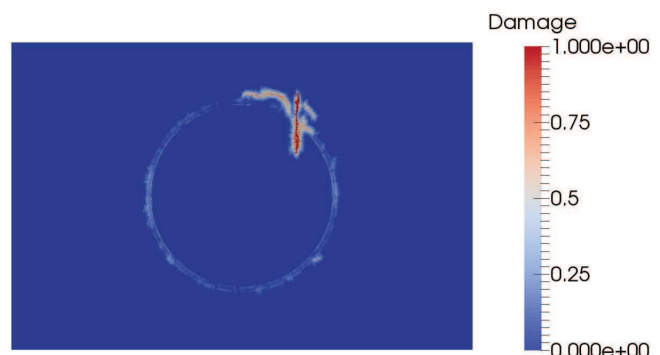


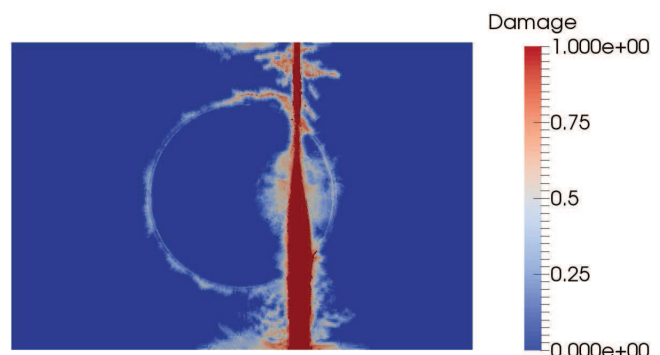
**Fig. 14 Magnitude of the electric field for the composite capacitor model at  $0.5 \mu\text{s}$**



(a)

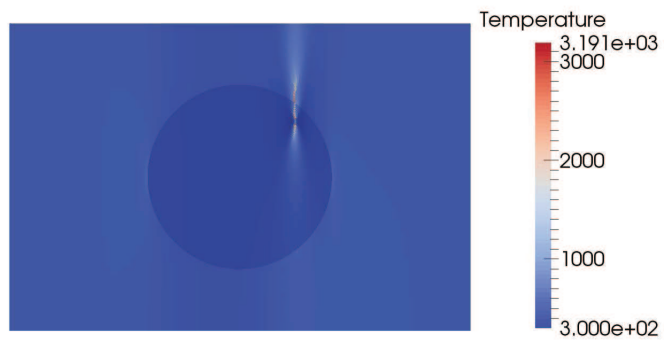


(b)

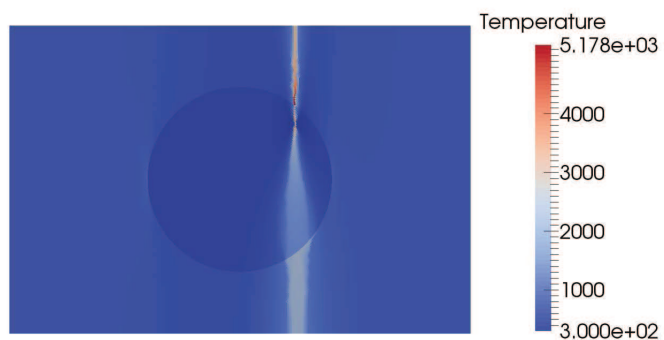


(c)

**Fig. 15 Peridynamic damage in the composite capacitor model at 5  $\mu$ s a), 5.5  $\mu$ s b), and 6  $\mu$ s c)**

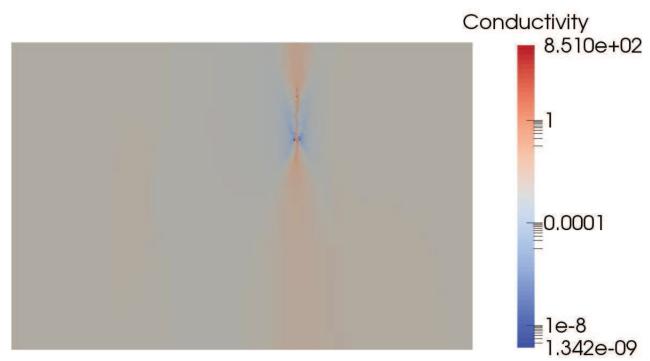


(a)

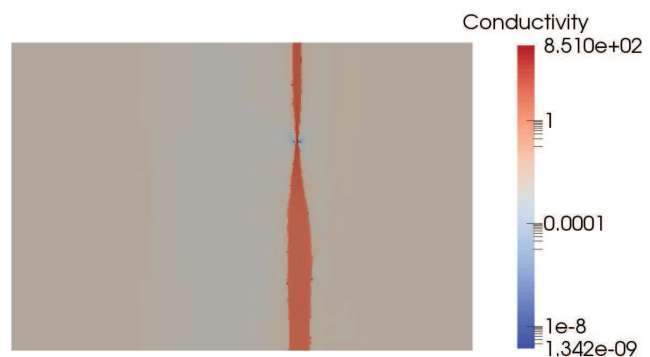


(b)

**Fig. 16** Temperature in the composite capacitor at 5.5  $\mu$ s a) and 5.5  $\mu$ s b)



(a)



(b)

**Fig. 17 Conductivity in the composite capacitor at 5.5  $\mu$ s a) and 5.5  $\mu$ s b)**

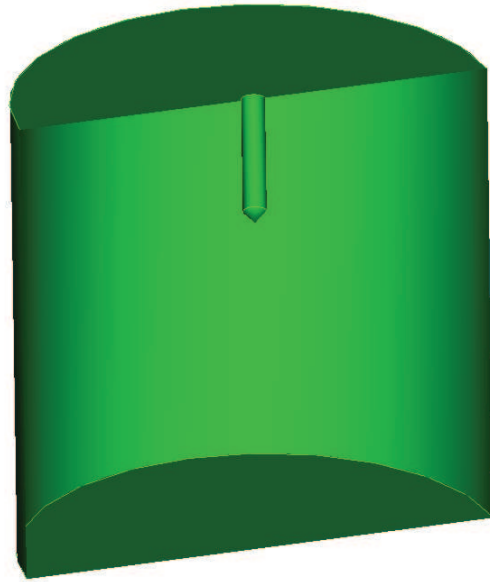


**Fig. 18 Cylindrical point–plane model (cutaway)**

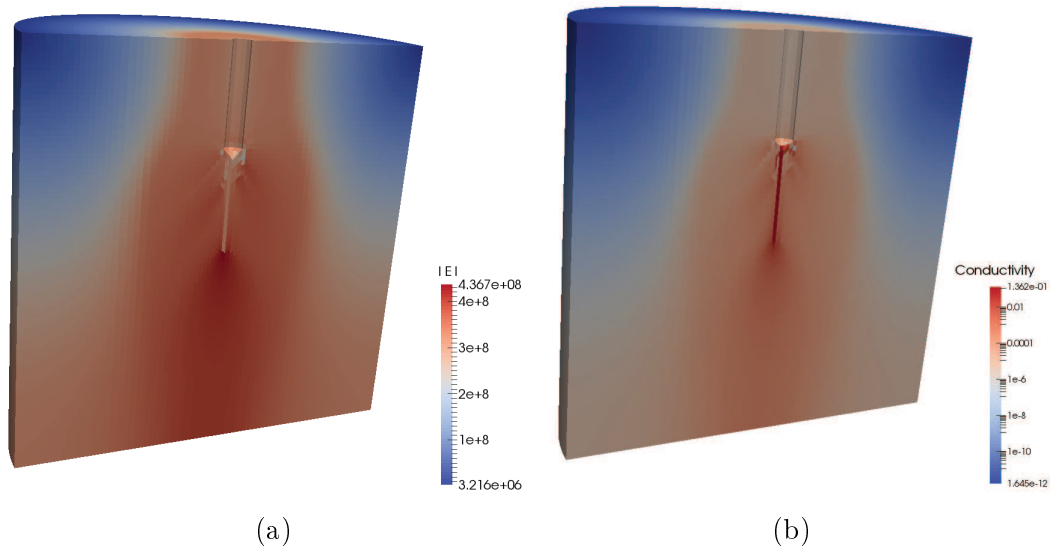


**Fig. 19 Electric-field magnitude a) and conductivity b) in the 3-D point–plane model at 2.2  $\mu$ s**

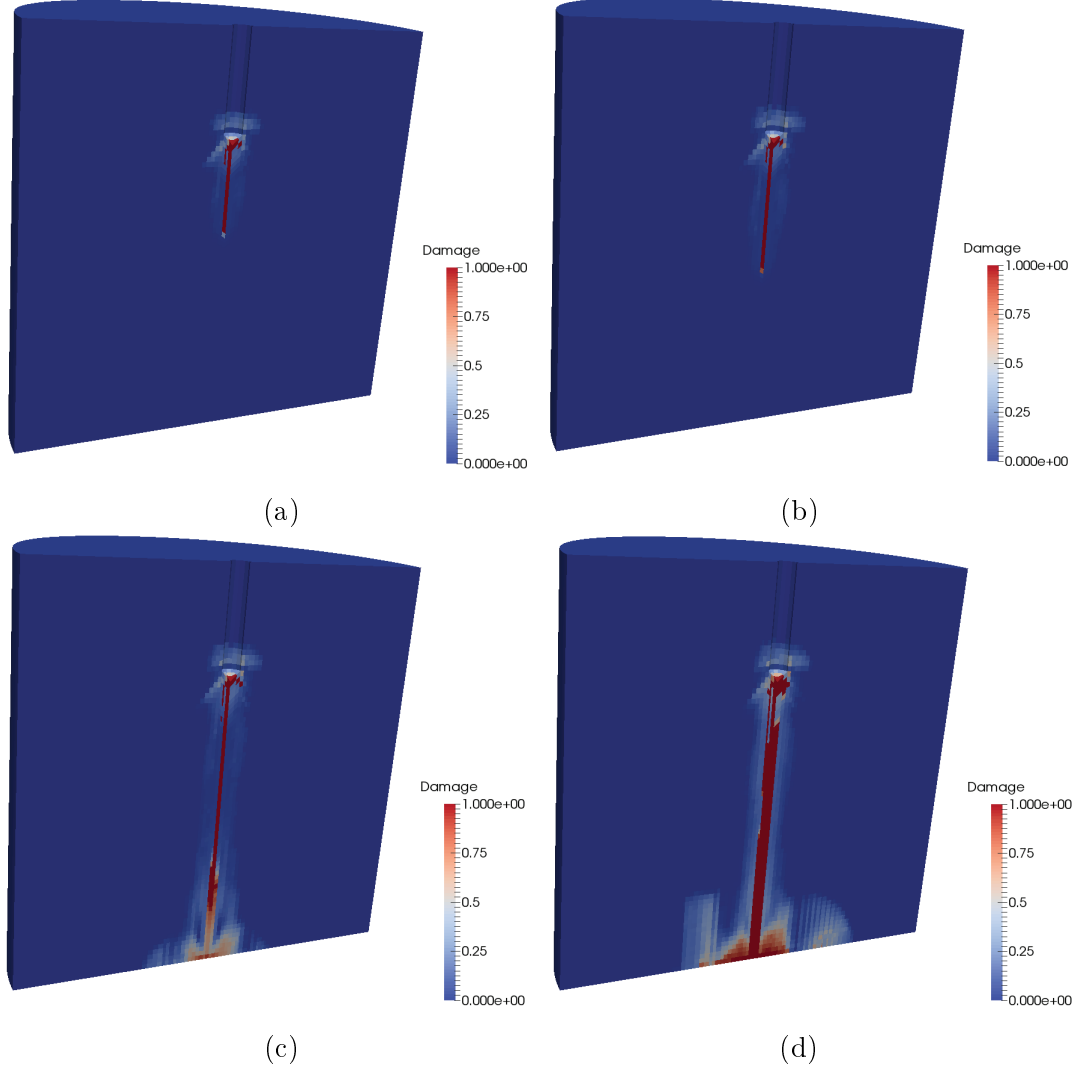


**Fig. 20 Peridynamic damage in the 3-D point–plane model at 2.25  $\mu$ s a), 3  $\mu$ s b), 3.75  $\mu$ s c), and 4.5  $\mu$ s d)**

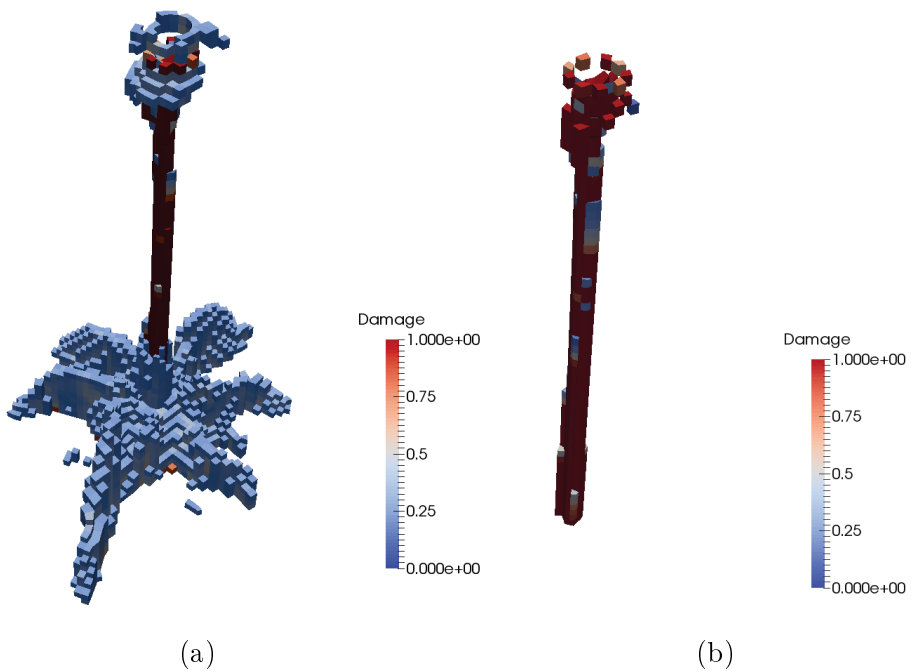


**Fig. 21 Peridynamic damage in the 3-D point–plane model at 4.5  $\mu$ s shown with a threshold on damage a) and temperature b)**

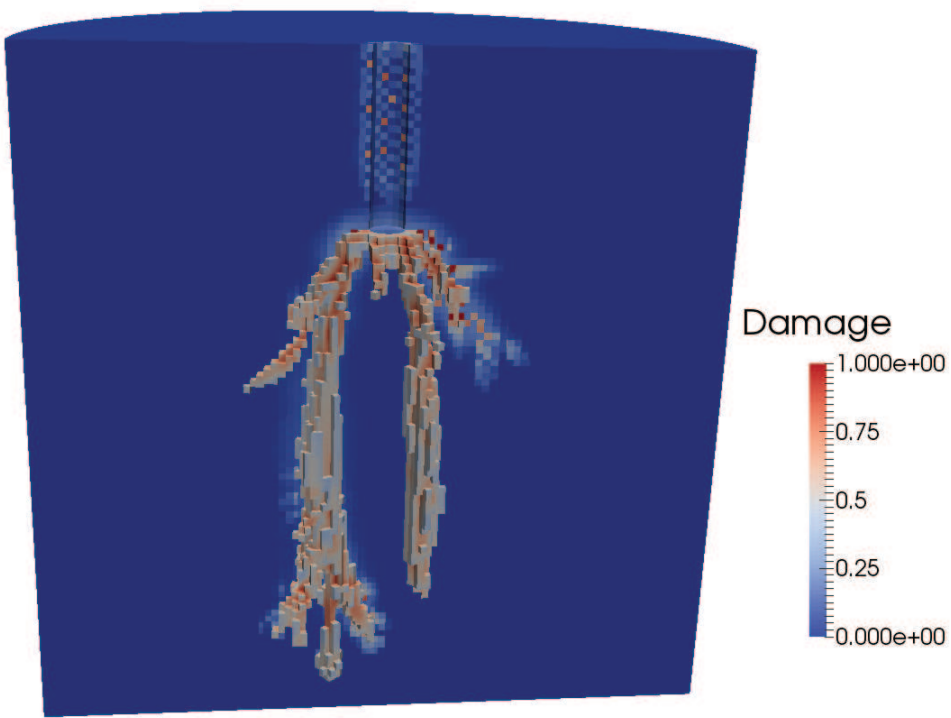


**Fig. 22** Damage for the flat-tipped probe in 3-D at  $3.3 \mu\text{s}$

## 6. References

---

1. O'Brien D, Baechle D, Yurchak O, Wetzel E. Effect of processing conditions and electrode characteristics on the electrical properties of structural composite capacitors. *Comp Part A: App Sci Manuf.* 2015;68:47–55.
2. Wildman R, Gazonas G. A dynamic electro-thermo-mechanical model of dielectric breakdown in solids using peridynamics. *J Mech Mat Struc.* 2015;10(5):613–630.
3. Silling S. Reformulation of elasticity theory for discontinuities and long-range forces. *J Mech Phy Sol.* 2000;48(1):175–209.
4. Silling S, Askari E. A meshfree method based on the peridynamic model of solid mechanics. *Comp Struc.* 2005;83(17-18):1526–1535.
5. Flynn PT. Field-dependent conductivity in non-uniform fields and its relation to electrical breakdown. *Proc IEE–Part C: Mono.* 1955;102(2):264–269.
6. Noskov M, Lopatin V, Cheglokov A, Shapovalov A. Computer simulation of discharge channel propagation in solid dielectric. In: Proc IEEE 7th Int Conf Solid Dielec.; p. 465–468.
7. Silling SA, Epton M, Weckner O, Xu J, Askari E. Peridynamic states and constitutive modeling. *J Elast.* 2007;88(2):151–184.
8. Du Q, Gunzburger MD, Lehoucq RB, Zhou K. A nonlocal vector calculus, non-local volume-constrained problems, and nonlocal balance laws. Sandia National Laboratories; 2010. Report No.: SAND-2010-8353J.
9. Neusel C, Jelitto H, Schmidt D, Janssen R, Felten F, Schneider GA. Dielectric breakdown of alumina single crystals. *J Euro Cer Soc.* 2012;32(5):1053–1057.

**INTENTIONALLY LEFT BLANK.**

## **List of Symbols, Abbreviations, and Acronyms**

---

---

1-D 1-dimensional

2-D 2-dimensional

3-D 3-dimensional

FE finite element

FEM finite element method

ODE ordinary differential equation

**INTENTIONALLY LEFT BLANK.**

1 (PDF)	DEFENSE TECHNICAL INFORMATION CTR DTIC OCA	85 (PDF)	DIR USARL RDRL CIH C E CHIN D GROVE J KNAP M LEE RDRL SE W BENARD RDRL-SED-P M BERMAN L BOTELER RDRL WM B FORCH S KARNA J LA SCALA A RAWLETT S SCHOENFELD J ZABINSKI RDRL WML A B BREECH RDRL WML B I BATYREV J BRENNAN E BYRD S IZVYEKOV J LARENTZOS W MATTSON B RICE D TAYLOR N WEINGARTEN RDRL WML G J O'GRADY RDRL WML H B AYDELOTTE C MEYER D SCHEFFLER B SCHUSTER RDRL WMM J BEATTY R DOWDING M VANLANDINGHAM RDRL WMM A D BAECHLE D O'BRIEN J TZENG RDRL WMM B B AKSOYLU T BOGETTI C DECKER C FOUNTZOULAS G GAZONAS D HOPKINS B LOVE
2 (PDF)	DIRECTOR US ARMY RESEARCH LAB RDRL CIO L IMAL HRA MAIL & RECORDS MGMT		
1 (PDF)	GOVT PRINTG OFC A MALHOTRA		
1 (PDF)	UNIV DELAWARE D WEILE		
1 (PDF)	UNIV NEBRASKA-LINCOLN F BOBARU		

B POWERS  
T WALTER  
R WILDMAN  
C YEN  
RDRL WMM D  
R BRENNAN  
A GAYNOR  
B MCWILLIAMS  
S WALSH  
J YU  
RDRL WMM E  
J LASALVIA  
J SWAB  
D SHREIBER  
RDRL WMM F  
E HERNANDEZ  
T SANO  
M TSCHOPP  
RDRL WMM G  
J ANDZELM  
J LENHART  
K MASSER  
C RINDERSPACHER  
T SIRK  
Y SLIOZBERG  
RDRL WMP  
D LYON  
RDRL WMP A  
S BILYK  
J CAZAMIAS  
RDRL WMP B  
S SATAPATHY  
M SCHEIDLER  
T WEERASOORIYA  
RDRL WMP C  
D CASEM  
J CLAYTON  
M FERMEN-COKER  
M GREENFIELD  
B LEAVY  
J LLOYD  
C MEREDITH  
S SEGLETES  
A SOKOLOW  
A TONGE  
C WILLIAMS  
RDRL WMP D  
R DONEY  
C RANDOW  
S SCHRAML  
M ZELLNER  
RDRL WMP E  
T JONES